Seismotectonics and stress field of the Yellowstone volcanic plateau from earthquake first-motions and other indicators

Gregory P. Waite and Robert B. Smith

Department of Geology and Geophysics, University of Utah, Salt Lake City, Utah, USA

Received 7 July 2003; revised 30 October 2003; accepted 14 November 2003; published 3 February 2004.

[1] We have found spatial variations in seismic stress indicators at the Yellowstone volcanic field, Wyoming, by examining source mechanisms of 25 years of network-recorded earthquakes, 1973–1998. Yellowstone seismicity is characterized by swarms of earthquakes ($M_C < 3$) within the 0.64 Ma Yellowstone caldera and between the caldera and the eastern end of the 44-km-long rupture of the 1959 M_S7.5 Hebgen Lake earthquake. We relocated more than 12,000 earthquake hypocenters using three-dimensional velocity models. Focal mechanisms calculated for 364 earthquakes, carefully selected for location accuracy, reveal predominantly normal faulting; however, fault orientations vary across the Yellowstone caldera. Specifically, focal mechanism *T* axes trend N-S in the vicinity of the Hebgen Lake earthquake fault zone NW of the Yellowstone caldera and rotate to ENE-WSW 35 km east of there. This rotation of the *T* axis trends occurs in the area of densest seismicity north of the caldera. Stress inversions performed using earthquake first-motion data reveal a similar pattern in the minimum principal stress orientations. The extension directions derived from the focal mechanisms and stress inversions are generally consistent with extension directions determined from geodetic measurements, extension inferred from alignments of volcanic vents within the caldera, and extension directions determined from regional normal faults. The N-S trending Gallatin normal fault north of the caldera is a notable exception; we find extension to be perpendicular to the direction of past extension on the Gallatin fault in the area immediately south of it. We interpret this N-S extension north of the caldera to be related to postseismic viscoelastic relaxation in the upper mantle and lower crust following the Hebgen Lake earthquake. The dominantly extensional tectonic regime at Yellowstone inferred from these results demonstrates the influence of NE-SW Basin and Range extension in this area. *INDEX TERMS:* 7215 Seismology: Earthquake parameters; 7230 Seismology: Seismicity and seismotectonics; 7280 Seismology: Volcano seismology (8419); *KEYWORDS:* stress field, focal mechanism, Yellowstone

Citation: Waite, G. P., and R. B. Smith (2004), Seismotectonics and stress field of the Yellowstone volcanic plateau from earthquake first-motions and other indicators, *J. Geophys. Res.*, *109*, B02301, doi:10.1029/2003JB002675.

1. Introduction

[2] The silicic Yellowstone volcanic field of is one of the largest active caldera systems in the world. Yellowstone's youthful volcanic history is marked by three cataclysmic, caldera-forming eruptions at 2.0, 1.3, and 0.64 Ma. The most recent of these eruptions formed a 45 km by 70 km collapse caldera that subsided up to 500 m along caldera rim normal faults [*Christiansen*, 2001]. Twenty-nine smaller rhyolite eruptions and ash flows have since filled the caldera. Although the last such rhyolite eruption occurred 70,000 years ago [*Christiansen*, 2001], the combined convective and conductive heat flux that drives Yellowstone's world famous hydrothermal system is more than 30 times the average heat flow of the North American continent [*Fournier*, 1989]. This high heat flow is interpreted to reflect crystallization of partial melt of rhyolite or basaltic magma in a midcrustal magma body that underlies the caldera [*Fournier*, 1989; *Miller and Smith*, 1999; *Husen et al.*, 2004]. In addition, the Yellowstone volcanic field has experienced extended periods of caldera-wide crustal deformation that demonstrate the volcano's unrest.

[3] The seismic history of Yellowstone is punctuated by the largest historic earthquake in the Rocky Mountains; the 19 August 1959 M_S7.5 Hebgen Lake, Montana earthquake produced a multiple-fault scarp up to 6 m high beginning 20 km NW of the caldera boundary [*Doser*, 1985] (see Figure 1 for locations of named geological and geographic features). This large normal fault system continues to extend N-S at 4 mm/yr as determined from Global Positioning System (GPS) measurements more than four decades after the earthquake [*Puskas et al.*, 2002].

[4] The 1975 M_L6.1 Norris Junction earthquake was the largest recorded event to occur within the Yellowstone caldera. *Pitt et al.* [1979] computed a composite, first-

0148-0227/04/2003JB002675$09.00

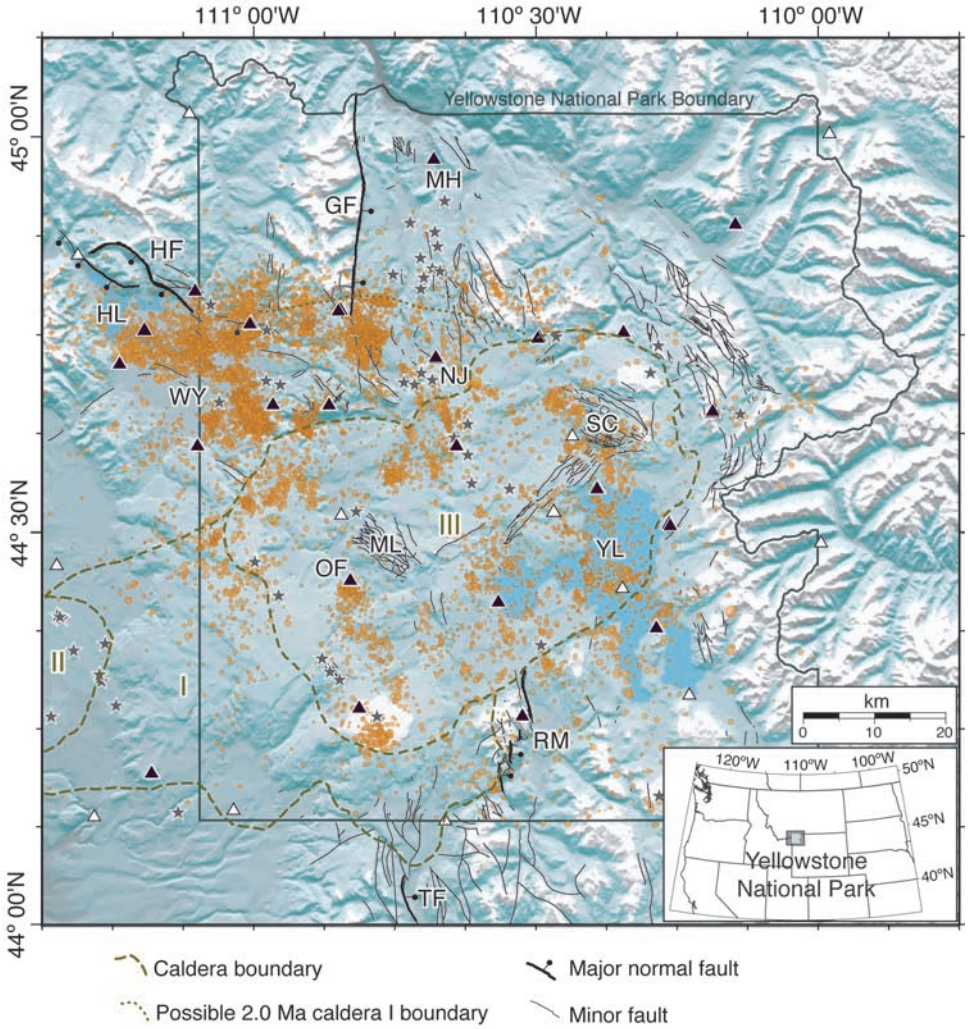

Figure 1. Index map of Yellowstone earthquake epicenters relocated with the three-dimensional velocity models of [*Miller and Smith*, 1999], seismograph network station distribution, late Quaternary faults [*Christiansen*, 2001], and postcaldera volcanic vents [*Christiansen*, 2001]. Earthquake epicenters for the period 1973 to 1998 are plotted as semitransparent dots to emphasize areas of highest seismicity. Seismograph stations that are operating are shown with a solid triangle; discontinued seismograph locations are marked with an open triangle. Two-letter abbreviations are as follows: Gallatin Fault (GF), Hebgen and Red Canyon Faults (HF), Hebgen Lake (HL), Mammoth Hot Springs (MH), Norris Junction and Hot Springs (NJ), Old Faithful (OF), Red Mountain Fault Zone (RM), Teton Fault (TF), and Yellowstone Lake (YL). Bold roman numerals indicate the locations of the 2.0, 1.3, and 0.64 Ma Yellowstone calderas as mapped by *Christiansen* [2001] which are outlined with bold black lines and labeled I, II, and III respectively.

motion focal mechanism from the main shock and aftershocks. The mechanism has a normal faulting solution with a NE trending *T* axis. Waveform modeling by *Bache et al.* [1980] produced a focal mechanism with a minor strike-slip component and a similar *T* axis orientation to that of *Pitt et al.* [1979]. While both the Hebgen Lake earthquake and the Norris Junction earthquake were primarily normal-faulting events, the fault orientations and rupture directions were markedly different.

[5] The well-recorded background seismicity is distinguished by clusters of small, shallow earthquakes, especially NW of the caldera. Yellowstone has been the most seismically active region of the 1300-km-long Intermountain Seismic Belt in historic time [*Smith and Sbar*, 1974] and is part of a pattern of epicenters that defines a parabolic zone of seismicity around the Yellowstone hot spot. The zone extends generally E-W through Idaho, north of the aseismic eastern Snake River Plain (SRP),to the north rim of the Yellowstone caldera and wraps around the SRP through the Teton fault zone and back to the west [*Smith and Siegel*, 2000; *Smith and Braile*, 1994]. The seismic belt continues south along the east boundary of the Basin and Range province through Utah and into northern Arizona.

[6] Geodetic surveys have revealed considerable vertical crustal deformation of the caldera and surrounding area. Studies using precise leveling first revealed caldera-wide uplift of up to 1 meter between 1923 and 1984 [*Pelton and*

Smith, 1982; *Dzurisin and Yamashita*, 1987]. Following this extended period of uplift, the caldera subsided more than 190 mm from 1985 through 1995 [*Dzurisin et al.*, 1994; *Puskas et al.*, 2002]. More recent satellite interferometric synthetic aperture radar and GPS studies, which provide improved spatial and temporal resolution, have revealed localized uplift and subsidence within and adjacent to the caldera [*Wicks et al.*, 1998; *Puskas et al.*, 2002]. *Waite and Smith* [2002] show a relationship between the largest earthquake swarm in Yellowstone and the 1985 deformation reversal. They suggest a rupture in a sealed system above the solidifying magma bodies released fluids into the shallow crust and triggered the swarm earthquakes. The migration of fluids from beneath the caldera may explain the subsidence.

[7] A previous study of Yellowstone earthquake focal mechanisms and stresses using data from 1973 to 1989 revealed overall NNE-SSW extension NW of the caldera [*Peyton*, 1991]. The sparse seismicity within the caldera limited *Peyton*'s [1991] study to earthquakes located NW of the caldera. Geodetic studies have confirmed NNE-SSW extension across the Hebgen Lake fault zone [*Dzurisin et al.*, 1990; *Savage et al.*, 1993; *Puskas et al.*, 2002]. Further, results from permanent and campaign GPS deployments show a rotation of extension from NNE-SSW in the Hebgen Lake region to ENE-WSW south of the Yellowstone caldera [*Puskas et al.*, 2002].

[8] We endeavored to explore the rotation in the stress field at Yellowstone implied by the large earthquake focal mechanisms and geodetic data using earthquake focal mechanisms and stress inversions of earthquake first-motion data. We computed 364 focal mechanisms constrained to be double couple from the 12,312 earthquakes recorded from 1973 to 1998 and relocated with three-dimensional velocity models from *Miller and Smith* [1999]. First-motion data from these events were inverted for the principal stress directions in eight areas with high seismicity north of the caldera.

2. Earthquake Data

[9] The earthquake data used in this study are from the University of Utah Seismograph Stations (UUSS) catalog. This includes data recorded by the U.S. Geological Survey for the period 1973 through 1981 [*Pitt*, 1987] and the UUSS from 1984 to 1998. The network comprised an average of 20 short-period stations from 1973 through 1981. In recent years, three-component short-period and broadband stations have been added to the network. At present, the network consists of three three-component broadband stations, three three-component short-period stations, and 18 vertical component short-period stations. Earthquakes were relocated using the three-dimensional velocity models determined from local earthquake and controlled source tomography by *Miller and Smith* [1999]. Figure 1 shows the earthquake epicenters as well as locations of the seismograph stations that have made up the Yellowstone network. The epicenters are plotted as semitransparent dots so that areas with dense seismicity are darker than areas with sparse seismicity. Earthquake magnitudes in the catalog range from M_C6.1 to below M_C0.0 (M_C refers to coda duration magnitude used in routine earthquake reporting by the UUSS).

[10] The most seismically active area of Yellowstone is to the north of the caldera between Norris Junction and Hebgen Lake. The deepest earthquakes, at 12 km depth, occur in this area. There are far fewer earthquakes within the caldera and most are less than 6 km deep. Seismicity is generally diffuse within and south of the caldera except for small clusters of events on the SW caldera boundary, beneath Yellowstone Lake, and south of Old Faithful. The shallow maximum earthquake depth within the caldera has been attributed to elevated temperature above cooling magma bodies resulting in decreased depth to the brittle-ductile transition [*Miller and Smith*, 1999].

3. Focal Mechanisms

3.1. Focal Mechanism Determination and Selection

[11] Yellowstone earthquakes are generally moderate to small (99.6% < M_C4) so that accurate first-motion determinations can often only be made on records from the nearest stations for a given event. We restricted focal mechanism determination to events with at least eight clear, first-motion picks. In order to ensure the most accurate focal depths for this study, we required that events must have a nearest station within 1.5 times the focal depth. Because Yellowstone earthquakes are generally shallow, especially within the caldera where focal depths are less than 6 km deep, this constraint left just 672 events, 32 of which had a nearest station within 1.0 times the focal depths. Station polarity reversal corrections were made where necessary from comparisons of the regional network data with well-recorded teleseisms (S. Nava, personal communication, 1998).

[12] Double-couple focal mechanism solutions for the selected events were determined using the nonlinear grid search program FPFIT [*Reasenberg and Oppenheimer*, 1985]. This code systematically varies values of strike, dip and rake over given intervals on a grid, and determines the normalized misfit between the planes and the observed first-motion data at each interval. The misfit is 0 if no observed first-motion polarities are inconsistent with the mechanism and 1 if all the stations are inconsistent.

[13] A trial set of focal mechanisms for each of the 672 events was found and stations with more than 25% first motions inconsistent with the mechanisms were removed. The mechanisms were recomputed and events that had multiple solutions with significant relative minima were removed. These multiple solutions are generally distinctly different from one another and indicate a poorly resolved solution. Finally, the uncertainties computed by FPFIT were used to remove the remaining poorly resolved focal mechanisms. We used the grading method described by *Gillard et al.* [1992] for a similar study of focal mechanisms in Hawaii to identify solutions of poor quality. Four parameters calculated by the program were used: the minimum misfit, and the uncertainty of the strike, dip, and rake angles. Seventy-two solutions with a misfit larger than 0.20 or an uncertainty in either strike, dip, or rake of more than 30° were rejected from the data set.

[14] The resulting final set of 364 mechanisms is plotted in Figure 2 along with focal mechanisms from the 1959 M_S7.5 Hebgen Lake main shock subevents [*Doser*, 1985] and the 1975 M_L6.1 Norris Junction earthquake [*Pitt et al.*, 1979]. More than 300 of the solutions are for earthquakes in

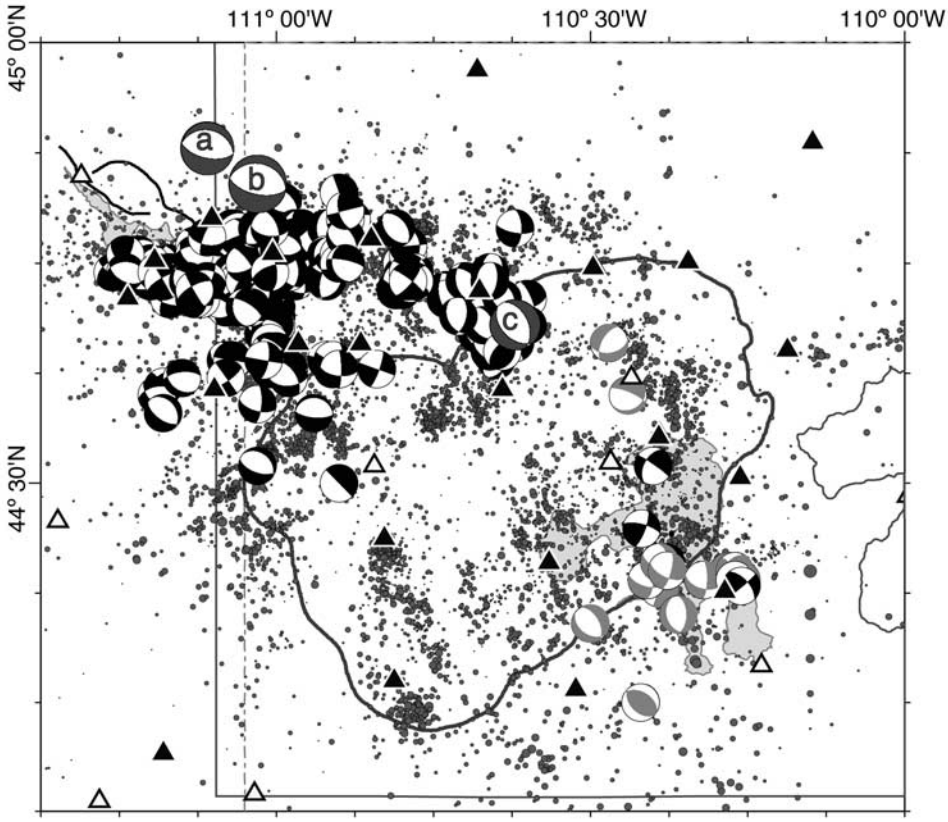

Figure 2. Complete set of 364 double-couple focal mechanism solutions for the period 1973 to 1998 plotted over the relocated epicenters (gray circles). The additional 18 events taken from a data set with less well constrained depths are plotted with gray compressional regions (see text). Larger mechanisms labeled a and b are 1959 M_S7.5 Hebgen Lake main shock subevents [*Doser*, 1985]. Mechanism c is a composite solution of the main shock and aftershocks of the 1975 M_L6.1 Norris Junction earthquake [*Pitt et al.*, 1979]. Seismograph stations are plotted as in Figure 1.

the region between the north rim of the caldera and Hebgen Lake fault, with few events inside the caldera. Because of the thin seismogenic zone within the caldera and less dense station spacing SE of the caldera, a small percentage of earthquakes in these areas fit the selection criteria. In order to increase the number of focal mechanisms in these poorly represented areas, additional focal mechanism solutions were computed with a relaxed quality constraint; for these 18 events, shown in gray in Figure 2, the distance from the epicenter to the nearest station was between 1.5 and 2 times the focal depth. They were otherwise filtered by the same methods described above. These additional data were not used in the stress inversions.

3.2. Double-Couple Focal Mechanism Results

[15] The mean number of first-motion observations per event used in the study is 10 and the average normalized misfit is 0.01. Over 90% of the solutions have a station distribution ratio of 0.5 or greater, indicating that the solutions are robust [*Reasenberg and Oppenheimer*, 1985]. The station distribution ratio is a measure of the distribution of the data on the focal sphere relative to the theoretical radiation pattern. A higher station distribution ratio indicates a larger number of stations in areas of large *P* wave amplitude and thus clear first motions. The average uncertainties in strike, dip, and rake as determined by the automated focal mechanism program are 9°, 13°, and 12°, respectively.

[16] The majority of the focal mechanisms determined in our study ranged between pure dip slip to pure strike slip; only a few thrust solutions were determined. The solutions were sorted into faulting types based on strike, dip, and rake orientation following the convention of *Aki and Richards* [1980] (Table 1). Because these categories are based on the fault slip angle, it was necessary to determine which of the two nodal planes was the fault plane in order to determine the proper rake. For each focal mechanism, the fault plane was chosen as the nodal plane that most closely matched the orientation of faults in the vicinity mapped and compiled by *Christiansen* [2001]. In most cases, the faulting type was the same regardless of which nodal plane was assumed to be the fault plane. A total of 148 events were found to be oblique normal, 100 normal, 99 strike slip, 12 oblique reverse, and 5 reverse.

[17] Horizontal projections of the compression (*P*) and tension (*T*) axes in Figure 3 show remarkable trends in orientation. The majority of the *P* axes are at angles close to vertical so the surface projections appear small. They trend approximately E-W in the Hebgen Lake region and most of the area north of the caldera rim. In the area around

Table 1. Event Types[a]

Rake Angle	Type of Faulting	Unconstrained	Constrained
$22.5° \geq$ rake $> -22.5°$	left-lateral strike-slip	45 (12%)	48 (14%)
$-22.5° \geq$ rake $> -67.5°$	oblique-normal left-lateral strike-slip	39 (11%)	79 (24%)
$-67.5° \geq$ rake $> -112.5°$	normal	100 (27%)	91 (27%)
$-112.5° \geq$ rake $> -157.5°$	oblique-normal right-lateral strike-slip	109 (30%)	57 (17%)
$-157.5° \geq$ rake $> 157.5°$	right-lateral strike-slip	54 (15%)	48 (14%)
$157.5° \geq$ rake $> 112.5°$	oblique-reverse right-lateral strike-slip	6 (2%)	1 (0%)
$112.5° \geq$ rake $> 67.5°$	reverse	5 (1%)	3 (1%)
$67.5° \geq$ rake $> 22.5°$	oblique-reverse left-lateral strike-slip	6 (2%)	5 (2%)

[a]Note that not all the unconstrained mechanisms were used in the inversions so the total number of constrained focal mechanisms (332) is smaller than the total number of unconstrained mechanisms (364).

Yellowstone Lake, the *P* axes are nearly N-S. The surface projections of the *T* axes, which are generally near horizontal, clearly illustrate a rotation from NNE-SSW near Hebgen Lake to ENE-WSW in the vicinity of Yellowstone Lake. This is consistent with larger-scale studies of the regional tectonics [e.g., *Zoback and Zoback*, 1989] and the orientations of Quaternary faults [*Christiansen*, 2001]. These directions are also consistent with geodetic results. In particular, GPS monitoring [*Puskas et al.*, 2002] shows extensional strain rotation similar to the observed rotation of the *T* axes.

4. Stress Field Solutions From Focal Mechanisms

4.1. Stress Inversion Method

[18] Several authors have developed procedures for resolving the stress field from a large number of individually determined focal mechanisms [e.g., *Angelier*, 1984; *Gephart and Forsyth*, 1984; *Michael*, 1984]. Other authors have solved for the stress field directly from the *P* wave polarity data and takeoff angles used to calculate focal mechanisms [e.g., *Rivera and Cisternas*, 1990; *Horiuchi et al.*, 1995; *Robinson and McGinty*, 2000; *Abers and Gephart*, 2001]. Using the polarity and takeoff angle data directly prevents any possible error in the fault plane solutions from being introduced into the stress field computations [*Horiuchi et al.*, 1995]. In addition, uncertainties can be applied to the first-motion data to provide a better estimate of the true error in the stress tensor model.

[19] *Horiuchi et al.* [1995] did not incorporate a means of error assessment into their first motion inversion code. Error estimation is possible using resampling [e.g., *Efron and Tibshirani*, 1986], but this is computationally expensive and we estimate months of computation time to compute 95% confidence intervals. *Robinson and McGinty* [2000] use resampling to calculate error estimates and require a priori selection of the coefficient of friction, a task that may be difficult in Yellowstone due to the hydrothermal system. *Rivera and Cisternas* [1990] did include an error estimate, but they solved a linearized approximation of this nonlinear inversion problem which can result in unrealistic error estimates.

[20] We employed *Abers and Gephart*'s [2001] algorithm, which follows the grid search inversion technique of *Gephart* [1990] but uses *P* wave polarity data and takeoff angles directly instead of focal mechanisms as input. As with the previously mentioned methods, it assumes that the earthquake generating stress is homogeneous throughout the inversion volume in both space and time and no a priori fault orientation information is assumed. The fault slip direction is defined to be parallel to the direction where shear stress is maximized. With this method, the first-motion data are weighted based on the probability of a pick being correct, permitting a better estimate of the full error in the stress solution. The highest weights are given to data farthest from the nodal planes where the theoretical *P* wave amplitude is largest and the probability of a mispick should be lowest.

[21] Two parameters describe the probability that the pick is correct. The first, α, is approximately the theoretical *P* wave amplitude below which pick reliability drops off considerably (near nodal planes). The second, γ is the overall estimate of mispicked data and is based on the fraction of inconsistent first motions in the entire data set. Tests of synthetic data show that these parameters have a considerable effect on the confidence bounds, as expected, and little effect on the best fit solution [*Abers and Gephart*, 2001]. Their synthetic tests were done using events with 15 uniformly distributed, noise-free first motions. Our data set consists of events with an average of 10 first motions that are not generally uniformly distributed. We tested the sensitivity of the stress solutions with a range of values from $0.01 \leq \alpha \leq 0.1$ and $0.01 \leq \gamma \leq 0.1$ and found little variation in the location of the best fitting principal stresses over these ranges. The changes in the best fit solutions are insignificant at the 95% confidence interval.

[22] The final values for parameters α and γ were estimated by fitting an error model though a set of points representing the fraction of correct picks over a range of radiation amplitudes for our entire set of focal mechanisms (Figure 4). The error model provides an estimate of the probability of a mispick for each radiation pattern amplitude:

$$p = \gamma + (1 - 2\gamma)\left(1 - 0.5e^{-|A|/\alpha}\right) \quad (1)$$

where $|A|$ is theoretical amplitude. It ranges from 0.5 at the nodal planes and approaches $(1 - \gamma)$ at the *P* and *T* axes (see Appendix A of *Abers and Gephart* [2001] for further explanation of the model). We find reasonable fits to the data with this model for low values of α (0.01–0.03) and γ (0.02–0.05). These output α and γ values depend somewhat on the input α and γ we use for generating the focal mechanisms so we conservatively choose $\alpha = 0.05$ and $\gamma = 0.05$ for the final focal mechanism and stress tensor calculations. These conservative values should ensure that accurate stress axis uncertainties are computed. *Abers and Gephart* [2001] suggest fixing $\alpha = 0.10$ and finding the best fitting γ using the error model. This is based in part on their

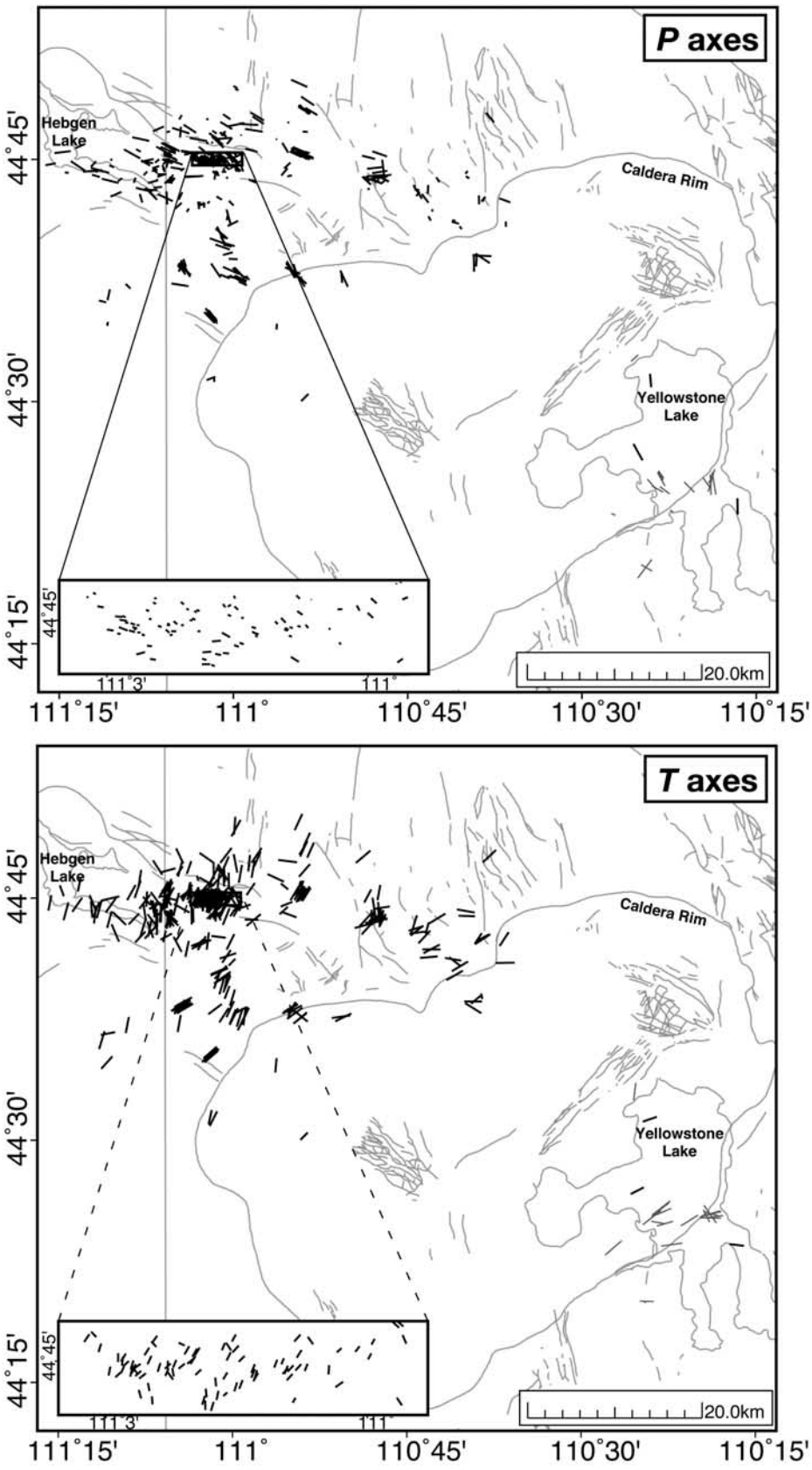

Figure 3. Surface projections of *P* and *T* axes from focal mechanism solutions. The boxes in the lower left are enlarged images of the region of the intense March 1977 swarm. The caldera III boundary, late Quaternary faults, and lake outlines are shown with fine lines.

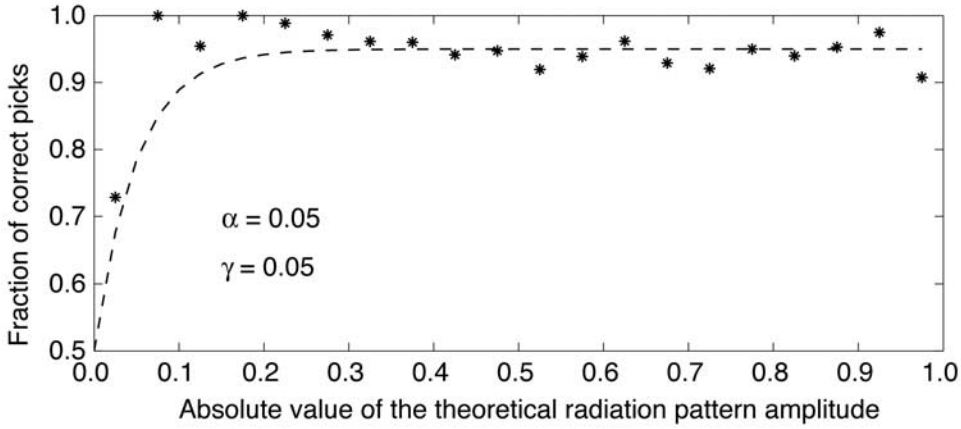

Figure 4. Plot of the fraction of correct picks over theoretical amplitude ranges used to determine the estimates of first-motion pick uncertainties. The stars are the actual fractions of correct picks for each amplitude range and the dashed line is the model fit to the data using $\alpha = \gamma = 0.05$. These values conservatively overestimate the data uncertainty at small amplitudes.

experience with the Southern California Earthquake Center catalog. Because we use three-dimensional velocity models to compute hypocenter locations and takeoff angles, a lower value for α is acceptable.

[23] The stress inversion algorithm solves for the orientation of the three principal stresses and the ratio of the stress magnitudes, $R = (\sigma_1 - \sigma_2)/(\sigma_1 - \sigma_3)$, by searching over a grid of values for each parameter. The weighted number of picks, S, consistent with each orientation of the principal stresses and value of R is calculated for each earthquake. The best fitting stress field orientation for a population of earthquake data is that which is fit by the largest number of first-motion data yielding the highest total S. Statistical confidence estimates on the solutions are based on these numbers of consistent picks. We search over all possible values of stress orientation and stress magnitude ratio. R was permitted to vary from 0 ($\sigma_1 = \sigma_2$) to 1 ($\sigma_2 = \sigma_3$).

4.2. Stress Tensor Results

[24] A stress model computed from all 364 focal mechanisms has a 75° plunging, 336° trending σ_1, near-horizontal σ_3 trending 202°, and $R = 0.5$. The 95% confidence regions for both σ_1 and σ_3 are relatively small. The heterogeneous data density (see Figure 2) and the apparent rotation of horizontal extension evident in the T axis orientations (see Figure 3) across the Yellowstone region suggest that the deviatoric stress at Yellowstone varies spatially.

[25] *Abers and Gephart* [2001] describe a formal method for assessing whether the stress field in a volume is homogeneous by comparing the fit of focal mechanisms determined without regard to the stress field, S, with those constrained by the best fitting stress field, S'. Focal mechanisms are constrained by forcing the slip direction to be parallel to the maximum resolved shear stress direction. The hypothesis of a homogeneous stress tensor in a volume can be rejected at the 95% confidence level when the difference in fit scores between the unconstrained and constrained focal mechanism sets, $dS = (S - S')$, exceeds 2.32 [*Abers and Gephart*, 2001]. Constraining all of the focal mechanisms in the data set to one stress tensor significantly degrades the misfit so that $dS = 7.26$ indicating strong heterogeneity in the data set.

[26] The focal mechanism data were initially divided into smaller areas based on regions with similar T axis orientations to distinguish regions of relatively homogeneous stress. Stress model solutions were computed on the smaller areas and examined for homogeneity. If the stress model computed resulted in significant differences in the fit scores between the constrained and unconstrained focal mechanisms for that area (i.e., $dS > 2.32$), we reexamined the data and defined smaller or slightly different areas for the stress computation. In some cases, reducing size of a data area so that it was homogeneous caused a significant increase in the solution uncertainty so further subdivision was not done. Some diversity in the focal mechanisms is necessary to achieve a well constrained solution [*Abers and Gephart*, 2001].

[27] The final areas, the orientations of the σ_3 axes, and the epicenters of earthquakes used in the inversions are shown in Figure 5. The corresponding solutions as well as the P and T axes for the stress-constrained and unconstrained focal mechanisms are plotted in Figure 6. Table 2 lists the best fit models for each area. Some areas, such as within and south of the caldera, were too sparsely populated with accurately located earthquakes to compute a reliable stress tensor inversion so not all of the focal mechanism data were used in these inversions.

[28] The pattern of T axis rotation from N-S near the Hebgen Lake fault zone to ENE-WSW near Norris Junction is reflected in the stress-field σ_3 orientations (Figure 5). The maximum rotation is 59° from area C to area H, a distance of about 35 km; however, the σ_3 orientation for area H is poorly constrained. Elsewhere, σ_3 is well constrained and near horizontal everywhere. The σ_1 directions are fairly well-constrained except in areas F, G, and H. Areas near Hebgen Lake (A, B, C, and D) have σ_3 trending north and south similar to the T axis orientation of the 1959 Hebgen Lake main shock. In areas E, F, and G south and east of Hebgen Lake, σ_3 trends NE and SW. Area H, which encompasses the location of the 1975 Norris Junction earthquake has an ENE trending σ_3 parallel to the orientation of the focal mechanism T axis

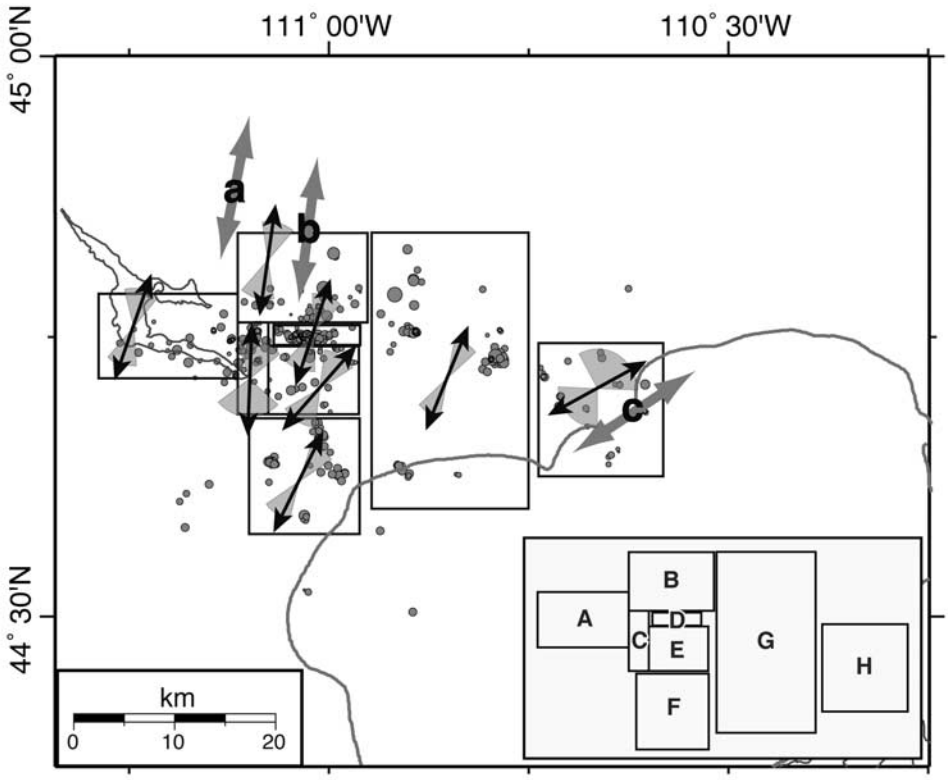

Figure 5. Map of areas that were used in stress tensor inversions. Epicenters of events for which focal mechanisms were determined are shown. Note that earthquakes that are not within the boxes were not used in the inversions. The thin black arrows indicate the direction of σ_3 for each area and the pie-shaped regions mark the 68% confidence intervals. The large gray arrows are the projections of the *T* axes from focal mechanisms of the 1959 M_S7.5 Hebgen Lake main shock subevents [*Doser*, 1985] and the 1975 M_L6.1 Norris Junction earthquake [*Pitt et al.*, 1979] shown in Figure 2.

computed for that event. The stress model for area H is poorly constrained and the 68% confidence region for σ_3 overlaps those of the other areas, but the good agreement of the best fit σ_3 with the GPS-derived direction of extension in that area, and the *T* axis of the Norris Junction earthquake give us some confidence that the rotation of σ_3 is realistic.

[29] Despite an effort to discriminate areas of homogeneous stress, four areas have large values of *dS*, indicating that stress homogeneity can be ruled out at the 95% confidence level. Areas C and D are the smallest spatially, yet have a large diversity in focal mechanisms. These areas separate the areas with N and S trending σ_3 from the areas of NE and SW trending σ_3, which may explain the apparent stress heterogeneities there. Area D has the highest value of *dS*, but the best constrained stress model. The diversity of mechanisms helps to constrain the stresses there. Conversely, area G is the largest spatially and includes 53 earthquakes, yet has a very low *dS* of 0.98.

[30] Two areas are dominated by earthquake swarms. Seventy-seven of the 87 events in area D occurred in a March 1977 swarm and 24 of the 43 earthquakes in area F were part of the autumn 1985 swarm, the largest earthquake swarm in the history of seismic network recording at Yellowstone. *Waite and Smith* [2002] performed separate inversions on two sets of events from area F: a set of events that were part of the autumn 1985 swarm and a set that were in the same plane as the swarm, but occurred in the year following the swarm. The earthquakes during the swarm showed a nearly horizontal $\sigma_1$with a trend subparallel to the NNW direction of swarm earthquake activity migration, while the postswarm earthquakes showed a nearly vertical σ_1. The orientation of σ_3 was similar for both sets of events. The rate of migration (115 m/d) away from the caldera, the rotation of σ_1, and the onset of caldera-wide subsidence that preceded the swarm suggest the swarm may have been triggered by a pressure pulse due to fluids migrating out of the caldera. No similar migrations of activity were identified for other swarms.

[31] Finally, we note that we explored possible temporal changes in the stress field associated with changes in caldera deformation noted by *Pelton and Smith* [1982], *Dzurisin and Yamashita* [1987], *Dzurisin et al.* [1994], and *Puskas et al.* [2002]. Small changes in the orientation of σ_1 were found, but we do not feel they are interpretable because the spatial distribution of earthquakes and seismographs varied with time. For example, the time period including the 1985 swarm is strongly influenced by those earthquakes, but few earthquakes occurred in that area prior to the swarm. It is not possible, therefore, to distinguish temporal changes from spatial variations.

4.3. Comparison of Stress-Consistent Focal Mechanisms With Unconstrained Focal Mechanisms

[32] We compare focal mechanism solutions that were constrained to have slip in the direction of maximum

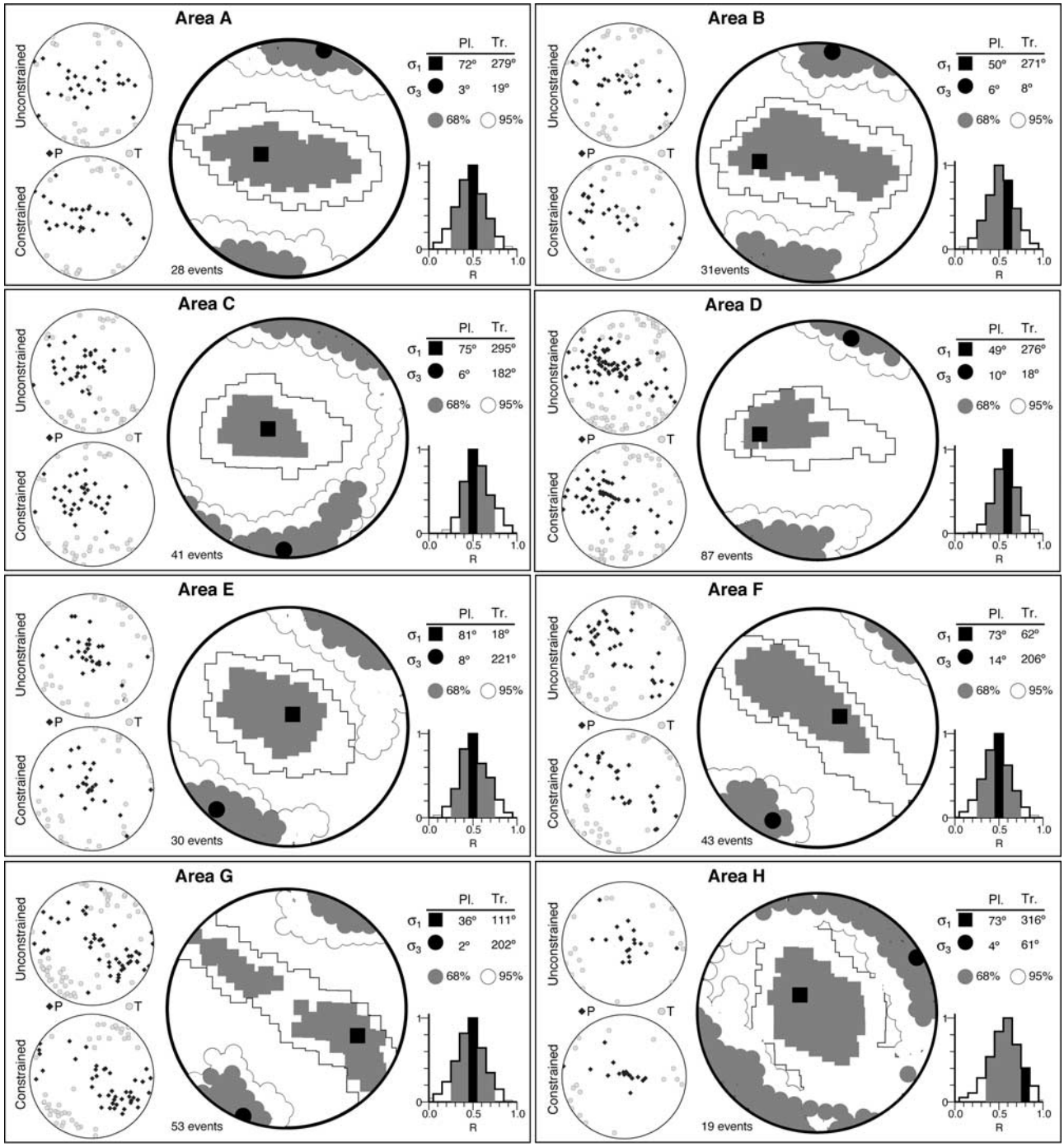

Figure 6. Stresses for the six areas within Yellowstone shown in Figure 5. *P* and *T* axes for all earthquakes in each area are shown for focal mechanisms unconstrained and constrained by the stress solution. Best fitting σ_1 and σ_3 are plotted with black square and circle, respectively. The plunge (Pl.) and trend (Tr.) of each is listed. The 68% confidence regions are shown in gray and the 95% confidence regions are white. Subdivisions were designed to minimize any possible heterogeneities in the stress field of the overall region. Areas were initially chosen based on areas of similar *T* axis orientations (see Figure 3).

shear stress with those computed independent of the stress field using two measures to quantify the differences. The first is the change in the data fit, *dS*, described above as a means for assessing the homogeneity of the stress in an area. Now we examine dS_j for individual mechanisms where j is the number of the event. The second is based on the change in focal mechanism orientation,

$$dM_j = 0.5*\left[(\mathbf{p}\bullet\mathbf{p}^{\mathbf{c}})^2+(\mathbf{t}\bullet\mathbf{t}^{\mathbf{c}})^2-(\mathbf{p}\bullet\mathbf{t}^{\mathbf{c}})^2-(\mathbf{t}\bullet\mathbf{p}^{\mathbf{c}})^2\right], \qquad (2)$$

Table 2. Results of Stress Inversions[a]

Area	NEv	NFM	σ_1 Pl., Tr.	σ_2 Pl., Tr.	σ_3 Pl., Tr.	dS	NdS_j > 1.0	NdM_j < 0.9
A	28	274	72°, 279°	17°, 110°	3°, 19°	1.31	1 (4%)	9 (32%)
B	31	274	50°, 271°	39°, 103°	6°, 8°	3.05	6 (19%)	13 (42%)
C	41	390	75°, 295°	14°, 91°	6°, 182°	4.60	5 (12%)	11 (27%)
D	87	893	49°, 276°	39°, 116°	10°, 18°	3.89	3 (3%)	25 (29%)
E	30	285	81°, 18°	4°, 130°	8°, 221°	3.01	0 (0%)	8 (27%)
F	43	400	73°, 62°	10°, 298°	14°, 206°	0.92	2 (5%)	7 (16%)
G	53	510	36°, 111°	54°, 295°	2°, 202°	0.98	1 (2%)	9 (17%)
H	19	181	73°, 316°	17°, 152°	4°, 61°	2.36	0 (0%)	3 (16%)

[a]NEv, number of events; NFM, number of first motions; NdS_j > 1.0, number of focal mechanisms that show a fit degradation when constrained by the stress field; NdM_j < 0.9, number of focal mechanisms that show a change in focal mechanism when constrained by the stress field.

where $\mathbf{p}$, $\mathbf{t}$, and $\mathbf{p^c}$, $\mathbf{t^c}$ are the unit vectors along the P and T axes for the unconstrained and constrained mechanisms for event j [*Abers and Gephart*, 2001]. Identical mechanisms have $dM_j = 1.0$ while mechanisms with opposite polarities, but identical fault planes (i.e., $\mathbf{p} = \mathbf{t^c}$ and $\mathbf{t} = \mathbf{p^c}$) have $dM_j = -1.0$.

[33] In each area, there are small changes in dS_j, but many events with changes in dM_j. This can be attributed to the small number of first motions available for each event. That is, it is possible to alter the orientations of the nodal planes without significantly degrading the fit of the first motions. While no events have $dS_j > 2.32$ (meaning the stress homogeneity assumption can be rejected for these events the 95% confidence level), the three areas with the largest dS each have an event with $dS_j > 2.0$. The number of events with $dS_j > 1.0$ in each area is listed in Table 2 ($dS_j = 1.0$ and $dS_j = 2.0$ correspond to confidence levels at which the stress homogeneity assumption can be rejected of 76% and 92%, respectively).

[34] Area B, which has the largest percentage of events with $dS_j > 1.0$ (19%), also has the largest percentage of events with $dM_j < 0.9$ (42%). Similarly, about 1/3 of the earthquakes in adjacent areas A, C, D, and E have $dM_j < 0.9$. Only about 1/6 of the earthquakes in the other areas have similar variations in the nodal plane orientations. The *P* and *T* axis plots in Figure 6 are also useful for examining the differences between the stress-constrained and unconstrained mechanisms. While it is difficult to track changes in individual mechanisms in these plots, constraining the mechanisms tends to cluster the *P* and *T* axes. The overall changes in mechanism types are also apparent from Table 1. The constrained mechanisms have a higher percentage of oblique-normal left-lateral strike-slip events and smaller percentage of oblique-normal right-lateral strike-slip events. All other categories are similar. The fault planes selected using the stress constraint do not, in general, align with mapped faults on the surface.

5. Discussion

[35] The Yellowstone volcanic field is located at the intersection of the three active late Cenozoic tectonic trends. North striking en echelon normal faults to the south of Yellowstone caldera, including the Teton Fault, and the north striking Gallatin Fault between Norris Junction and Mammoth Hot Springs indicate E-W extension [*Christiansen*, 2001]. Two alignments of postcaldera volcanic vents within the caldera (Figure 7) have been suggested as evidence of links between the extension structures north and south of the caldera [*Ruppel*, 1972; *Christiansen*, 2001]. East to SE striking faults to the west and NW of Yellowstone, including the Hebgen Lake and Red Canyon faults which ruptured in 1959, indicate extension is approximately N-S in that region [*Doser*, 1985]. Finally, the Yellowstone Plateau is also the terminus of the SRP, which is extending along its NE trend as evidenced by orientations of volcanic rift zones [*Smith et al.*, 1996; *Smith and Braile*, 1994] and GPS observations [*Puskas et al.*, 2002]. These features are plotted in Figure 7 along with the seismic stress and strain indicators computed for this study and the GPS-derived extensional strain directions from *Puskas et al.* [2002].

[36] The seismicity at Yellowstone is due to a combination of regional tectonics and local spatial and temporal variations in stress associated with active volcanic processes. On the smaller scale, changes in the volcanic system, such as the migration of fluids, may induce short-lived swarms of earthquakes [e.g., *Waite and Smith*, 2002]. On the larger scale, upper mantle dynamics may be important in defining the regional state of stress. The earthquakes in the region occur along a parabola that wraps around the eastern SRP with an axis of symmetry parallel to both the SRP and the direction of North America Plate motion. The parabola of seismicity correlates with topography as well. The seismically quiescent SRP has an elevation between 1200 m and 1600 m, while elevations in the mountainous seismic parabola exceed 3,500 m [*Smith and Braile*, 1994]. Several authors [e.g., *Anders and Sleep*, 1992; *Pierce and Morgan*, 1992; *Smith and Braile*, 1994] proposed that this pattern of seismicity is related to lateral spreading of a hot spot plume at the base of the lithosphere. If this is correct, the pattern of faulting will continue to migrate northeastward.

[37] The regional extension direction, inferred geologically from fault scarp striations, and in situ measurements [*Zoback*, 1992], is consistently E-W south of Yellowstone through central Utah perpendicular to the eastern boundary of the Basin and Range. Contemporary extensional strain directions from focal mechanisms and moment tensor solutions show more variation with NE-SW extension in the region immediately to the south of Yellowstone and approximately E-W extension through central Utah (Figure 8) [*Eddington et al.*, 1987; *Zoback*, 1992]. To the north and west of Yellowstone, geologically and seismically determined extension directions are generally NE-SW with locally more N-S extension in the area of the 1959 Hebgen Lake earthquake [*Doser*, 1985; *Eddington et al.*, 1987; *Zoback*, 1992; *Nabelek and Xia*, 1995]. The direction of extension in the Hebgen Lake area from GPS is NNE-SSW [*Puskas et al.*, 2002].

[38] In accordance with these large-scale extensional tectonic trends, *T* axes from earthquakes computed for this study show a rotation from approximately N-S in the Hebgen Lake region to ENE–WSW south of the Yellowstone caldera. The minimum principal stress directions rotate as well, but we do not have adequate data to constrain the stress direction within or south of the caldera. The highest seismicity at Yellowstone occurs in an E-W band adjacent to the eastern extent of rupture of the Hebgen Lake earthquake and a NW-SE band between Hebgen Lake and the caldera rim. The σ_3 direction is fairly uniform in that

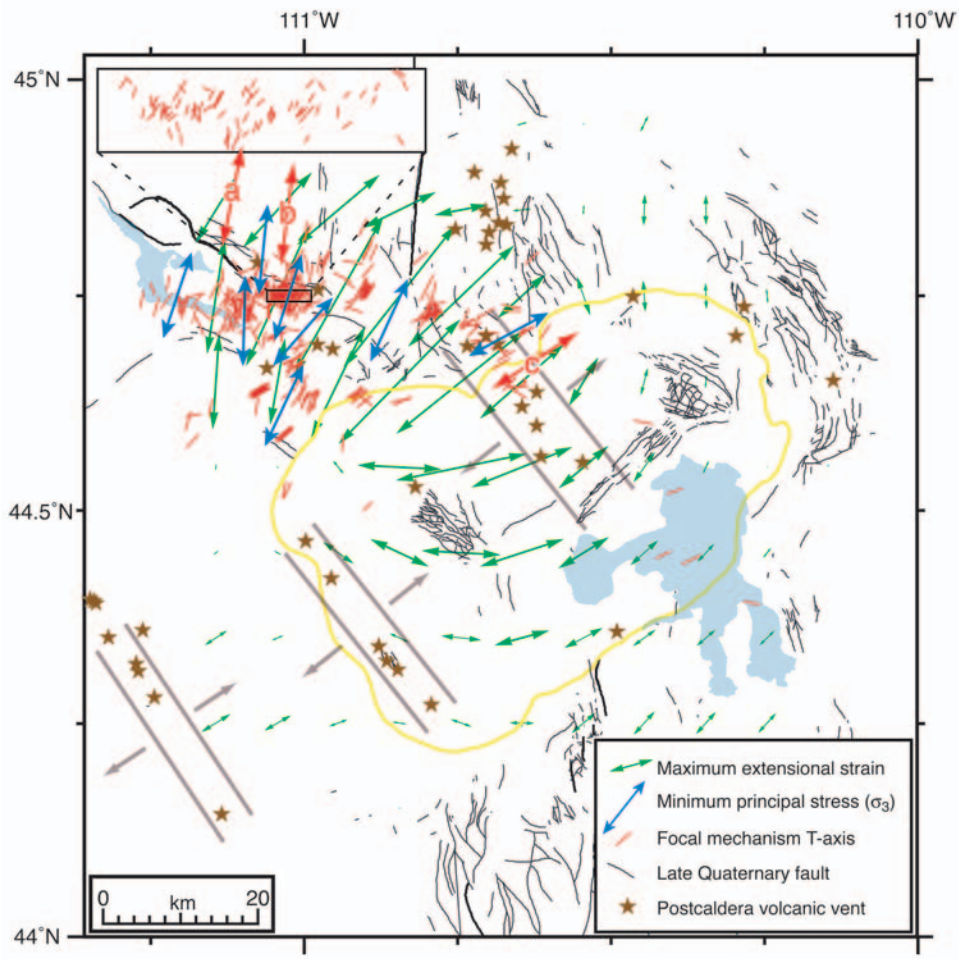

Figure 7. Seismic, geodetic, and geologic stress indicators across Yellowstone. *T* axes and σ_3 directions are as in Figures 3 and 5, respectively. The large red arrows labeled a, b, and c are *T* axes as in Figure 5. The green arrows are maximum extensional strain measured by GPS for the time period 1995–2000 [*Puskas et al.*, 2002] The lengths of the green arrows are proportional to the strain rate. Lines and arrows around the volcanic vents indicate the approximate extension direction that may be inferred from the alignments of the vents.

part of the E-W band to the west of Norris Junction (areas A, B, C, and D) and nearly parallel to the direction of extension across the Hebgen Lake fault zone measured by GPS [*Puskas et al.*, 2002] and trilateration [*Savage et al.*, 1993]. The earthquakes in this area are likely influenced by postseismic deformation of the 1959 Hebgen Lake earthquake.

[39] *Chang and Smith* [2002] modeled the coseismic Coulomb failure stress (CFS) changes associated with the 1959 Hebgen Lake earthquake and found most local earthquakes between 1959 and 1975 occurred in regions of increased CFS. The two lobes of increased CFS east and SE of the rupture also correspond with the two areas of highest seismicity in Yellowstone for the time period we examined from 1973 to 1998: the E-W band of high seismicity (areas A, B, C, and D) and the location of the 1985 swarm in area F, respectively. Area H, with a markedly different σ_3 orientation is just east of this lobe of increased CFS. For the time period of this study, 14–38 years after the Hebgen Lake earthquake, the coseismically induced changes in CFS may not have a strong influence on earthquakes, since prior earthquakes may have released the stress. However, it is likely that postseismic upper mantle and lower crustal viscoelastic relaxation modeled by *Chang et al.* [2002] from GPS observations of continuing extension across the Hebgen Lake fault is encouraging earthquakes in approximately the same areas that experienced increased CFS. Those areas that have N–S to NNE–SSW σ_3, which is approximately parallel to the direction of contemporary extension across the fault, are likely influenced by this postseismic relaxation. At the easternmost end of this band of seismicity (area H), the σ_3 direction rotates to ENE–WSW and there is little indication for an influence from the Hebgen Lake earthquake.

[40] As well as demonstrating the influence of postseismic deformation of the Hebgen Lake earthquake, the E-W band of seismicity may be an indication of a much older zone of weakness. The distinct topographic change between the seismically quiescent Paleozoic-cored Gallatin range immediately to the north of this area of highest seismicity may have resulted from the 2.0 Ma catastrophic eruption and may represent part of the northern extent of that caldera

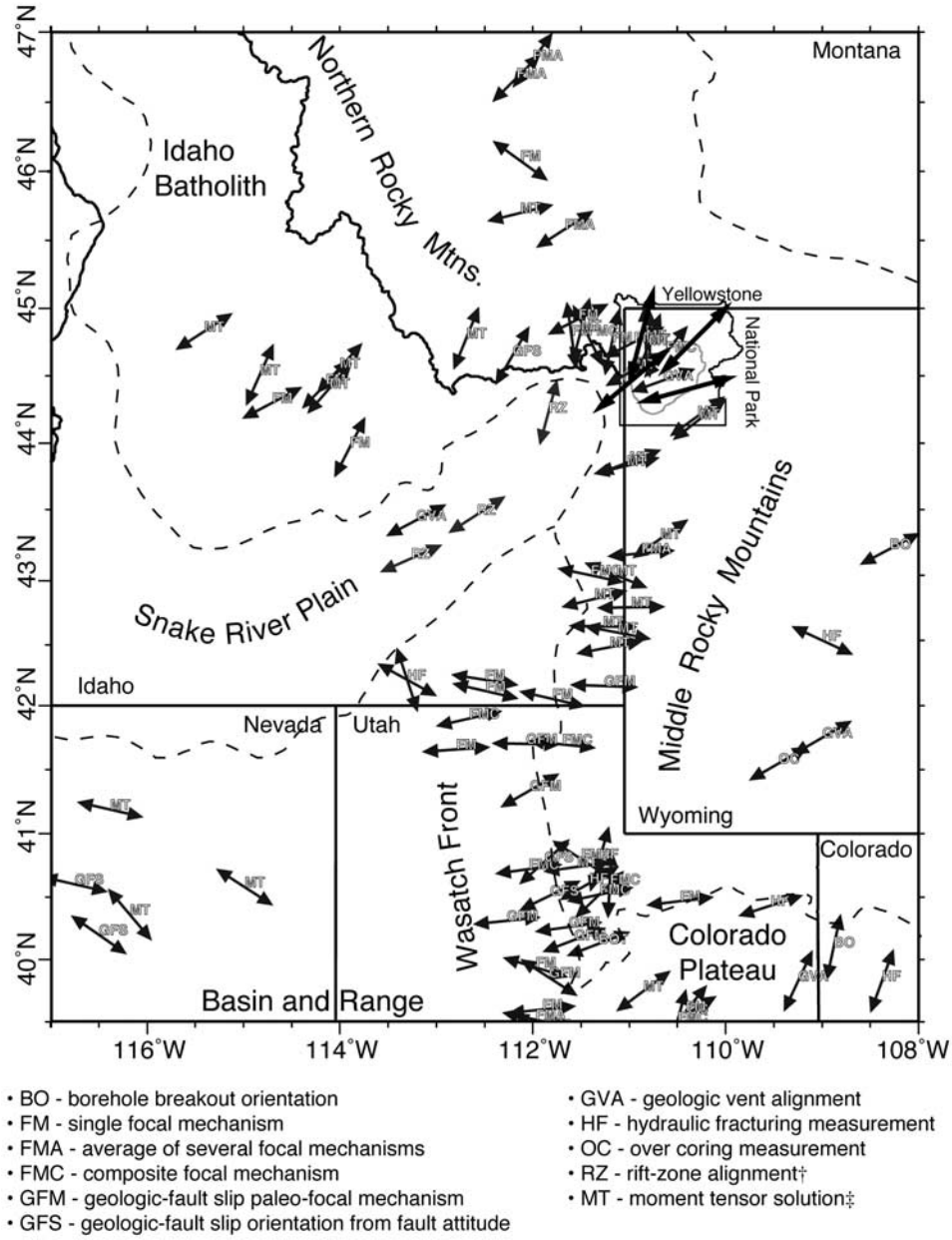

Figure 8. Summary of the horizontal projections of minimum principal stress directions for the northern Basin and Range, SRP, middle Rocky Mountains, and surrounding areas from various sources. The large, dark arrows in Yellowstone are average *T* axis directions from this study. All other data are modified after *Zoback* [1992] except RZ are after mapped rift zones from *Smith et al.* [1996] and MT are from Oregon State University moment tensor catalog [see *Nabelek and Xia*, 1995].

(caldera I in Figure 1). Some of earthquakes in the area could be occurring on caldera I boundary normal faults that have been buried by subsequent eruptions. The bedrock in most of this area is overlain by Quaternary sediments, so we can only estimate the location of the proposed caldera boundary based on the location of the band of seismicity and the southernmost extent of mapped geologic features older than 2.0 million years. This is shown as a dashed line in Figure 1. It is not clear how the caldera might connect with the western extent of the mapped caldera boundary.

[41] If the alignments of volcanic vents within the caldera are links between the extensional structures north and south of the caldera as has been suggested [*Ruppel*, 1972; *Christiansen*, 2001], then the orientation of those alignments indicate ENE extension within the caldera (Figure 7). The direction of maximum extension from GPS is consistent with extension inferred from the vent alignments in central caldera, but inconsistent in the southwestern caldera [*Puskas et al.*, 2002]. This ENE extension in the central caldera continues across the northern caldera boundary near Norris Junction. The focal mechanisms and zone of after-

shocks of the 1975 Norris Junction M_L6.1 earthquake indicate NE extension there and the minimum principal stress direction (area H) is consistent with the focal mechanisms and GPS observations.

[42] The apparent inconsistency of the GPS-derived extension directions in the southwestern caldera with the direction of extension implied by the volcanic vent alignment may be due to transient crustal deformation. The GPS data we examined were collected from 1995 to 2000, but GPS-derived extension directions from data collected between 1987 and 1995 show approximately NE-SW extension throughout the caldera. The extension directions in other areas are consistent in both time periods.

[43] In the southeastern part of the caldera near Yellowstone Lake, focal mechanism *T* axes trend E-W and ENE. North striking normal faults of the Red Mountain fault zone step eastward north of the Teton fault toward Yellowstone Lake. The E-W trends in *T* axes in this area may reflect the influence of these normal faults south of the Yellowstone caldera.

[44] The Gallatin fault is the major north striking normal fault north of the Yellowstone caldera and is associated with a 40-km-long Norris-Mammoth corridor subsidence structure east of the fault. This area contains the only major cluster of volcanic vents and hydrothermally altered areas outside the caldera and SRP, yet has had little seismic activity since at least the installation of the earthquake monitoring network in late 1972. Swarms are common just NW of the Norris area, but there have been no swarms and very little seismicity farther north along the Norris-Mammoth corridor. The lack of seismicity, combined with contemporary surface deformation measurements that show extension oblique to the fault [e.g., *Puskas et al.*, 2002], suggest E-W extension on the Gallatin fault has slowed or ceased.

6. Conclusions

[45] This study is the first to examine the spatially varying stress field at Yellowstone using the catalog of network-recorded earthquakes. We observe a rotation of extensional stress indicators north of the Yellowstone caldera in the areas where seismicity is the densest. Unfortunately, we are unable to resolve the state of stress within and south of the caldera because of the shallow nature of the seismicity there. The *T* axes from the few focal mechanisms we resolve there indicate extension is likely to be E–W. If the number of stations within the caldera were increased, more focal mechanisms could be resolved in the future.

[46] It has been suggested that N-S striking normal faults to the north and south of the Yellowstone caldera were continuous features that were interrupted by Yellowstone volcanism. The alignments of postcaldera volcanic vents within the 0.6 Ma caldera may represent zones of weakness linking the normal faults to the north and south. However, this study reveals minimum principal stress directions that indicate that the N-S striking normal faults to the north of the caldera may no longer be active. The E-W band of highest earthquake activity at Yellowstone includes some areas that have nearly N-S extension, which is nearly perpendicular to the extension direction of the Gallatin fault immediately north of that area. We suggest that the N-S extension may be related to viscoelastic relaxation in the upper mantle and lower crust following the 1959 Hebgen Lake earthquake. This N-S extension may represent a young kink in the continuous E-W extensional feature, possibly a result of the northeastward migration of the Yellowstone hot spot. Overall, the N–S to E–W extension inferred from these results is consistent with the interpretation that crustal deformation at Yellowstone is dominated by NE-SW Basin and Range extension in this area.

[47] **Acknowledgments.** This work was funded in part by U.S. Geological Survey grants 98-HQ-AG-2001 and 1434-95-A-01295, NSF Continental Dynamics Program Grant EAR-CD-9725431, and a University of Utah Graduate Research Fellowship. We thank the University of Utah Seismograph Station staff for assistance with data acquisition and analysis and the National Park Service for their cooperation in recording earthquakes in Yellowstone. Thanks also to John W. Gephart and Geoff Abers for the use of their stress inversion codes. Thank you to David P. Hill and Ronald L. Bruhn for assistance with the original manuscript. Some plots were created with GMT [*Wessel and Smith*, 1991] and Geotouch [*Lees*, 2000]. We also thank John Townend, Mary Lou Zoback, and John F. Cassidy for their comments and suggestions.

References

Abers, G. A., and J. W. Gephart (2001), Direct inversion of earthquake first motions for both the stress tensor and focal mechanisms and application to southern California, *J. Geophys. Res.*, *106*(B11), 26,523–26,540.

Aki, K., and P. G. Richards (1980), *Quantitative Seismology*, W. H. Freeman, New York.

Anders, M. H., and N. H. Sleep (1992), Magmatism and extension: The thermal and mechanical effects of the Yellowstone hotspot, *J. Geophys. Res.*, *97*(B11), 15,379–15,393.

Angelier, J. (1984), Tectonic analysis of fault slip data sets, *J. Geophys. Res.*, *89*(B7), 5835–5848.

Bache, T. C., D. G. Lambert, and T. G. Barker (1980), A source model for the March 28, 1975, Pocatello Valley earthquake from time-domain modeling of teleseismic *P* waves, *Bull. Seismol. Soc. Am.*, *70*(2), 405–418.

Chang, W.-L., and R. B. Smith (2002), Integrated seismic-hazard analysis of the Wasatch Front, Utah, *Bull. Seismol. Soc. Am.*, *92*(5), 1904–1922.

Chang, W.-L., R. B. Smith, C. M. Meertens, and C. M. Puskas (2000), Rheologic properties of an extending lithosphere from the inversion of postseismic deformation (EDM and GPS) of the 1959 Hebgen Lake, Montana, earthquake, *Eos Trans. AGU*, *83*(47), Fall Meet. Suppl., Abstract F635.

Christiansen, R. L. (2001), The Quaternary and Pliocene Yellowstone Plateau volcanic field of Wyoming, Idaho, and Montana, *U.S. Geol. Surv. Prof. Pap.*, *729-G*.

Doser, D. I. (1985), Source parameters and faulting processes of the 1959 Hebgen Lake, Montana, earthquake sequence, *J. Geophys. Res.*, *90*(B6), 4537–4555.

Dzurisin, D., and K. M. Yamashita (1987), Vertical surface displacements at Yellowstone caldera, Wyoming, 1976–1986, *J. Geophys. Res.*, *92*(B13), 13,753–13,766.

Dzurisin, D., J. C. Savage, and R. O. Fournier (1990), Recent crustal subsidence at Yellowstone Caldera, Wyoming, *Bull. Volcanol.*, *52*, 247–270.

Dzurisin, D., K. M. Yamashita, and J. W. Kleinman (1994), Mechanisms of crustal uplift and subsidence at the Yellowstone caldera, Wyoming, *Bull. Volcanol.*, *56*, 261–270.

Eddington, P. K., R. B. Smith, and C. Renggli (1987), Kinematics of Basin and Range intraplate extension, in *Continental Extensional Tectonics*, edited by M. P. Coward, J. F. Dewey, and P. L. Hancock, pp. 371–392, Blackwell Sci., Malden, Mass.

Efron, B., and R. Tibshirani (1986), Bootstrap methods for standard errors, confidence intervals, and other measures of statistical accuracy, *Stat. Sci.*, *1*, 54–77.

Fournier, R. O. (1989), Geochemistry and dynamics of the Yellowstone National Park hydrothermal system, *Annu. Rev. Earth Planet. Sci.*, *17*, 13–53.

Gephart, J. W. (1990), FMSI: A FORTRAN program for inverting fault/slickenside and earthquake focal mechanism data to obtain the regional stress tensor, *Comput. Geosci.*, *16*(7), 953–989.

Gephart, J. W., and D. W. Forsyth (1984), An improved method for determining the regional stress tensor using earthquake focal mechanism data: Application to the San Fernando earthquake sequence, *J. Geophys. Res.*, *89*(B11), 9305–9320.

Gillard, D., M. Wyss, and J. S. Nakata (1992), A seismotectonic model for western Hawaii based on stress tensor inversion from fault plane solutions, *J. Geophys. Res.*, *97*(B5), 6629–6641.

Horiuchi, S., R. Guillermo, and A. Hasegawa (1995), Discrimination of fault planes from auxiliary planes based on simultaneous determination of stress tensor and a large number of fault plane solutions, *J. Geophys. Res.*, *100*(B5), 8327–8338.

Husen, S., R. B. Smith, and G. P. Waite (2004), Evidence for gas and magmatic sources beneath the Yellowstone Volcanic Field from seismic tomographic imaging, *J. Volcanol. Geotherm. Res.*, in press.

Lees, J. M. (2000), Geotouch: Software for three and four dimensional GIS in the earth sciences, *Comput. Geosci.*, *26*(7), 751–761.

Michael, A. J. (1984), Determination of stress from slip data: faults and folds, *J. Geophys. Res.*, *89*(B13), 11,517–11,526.

Miller, D. S., and R. B. Smith (1999), *P* and *S* velocity structure of the Yellowstone volcanic field from local earthquake and controlled-source tomography, *J. Geophys. Res.*, *104*(B7), 15,105–15,121.

Nabelek, J., and G. Xia (1995), Moment-tensor analysis using regional data; application to the March 25, 1993, Scotts Mills, Oregon, earthquake, *Geophys. Res. Lett.*, *22*(1), 13–16.

Pelton, J. R., and R. B. Smith (1982), Contemporary vertical surface displacements in Yellowstone National Park, *J. Geophys. Res.*, *87*(B4), 2745–2761.

Peyton, S. L. (1991), Seismotectonics of the Yellowstone - Hebgen Lake region from earthquake focal mechanisms and stress field inversions, M.S. thesis, Univ. of Utah, Salt Lake City.

Pierce, K. L., and L. A. Morgan (1992), The track of the Yellowstone hot spot; volcanism, faulting, and uplift, in *Regional Geology of Eastern Idaho and Western Wyoming*, edited by P. K. Link, M. A. Kuntz, and L. B. Platt, *Mem.Geol. Soc. Am.*, *179*, 1–53.

Pitt, A. M. (1987), Catalog of earthquakes in the Yellowstone National Park - Hebgen Lake Region, Wyoming, Montana, and Idaho, for the years 1973 to 1981, *U.S. Geol. Surv. Open File Rep.*, *87-611*, 65 pp.

Pitt, A. M., C. S. Weaver, and W. Spence (1979), The Yellowstone Park earthquake of June 30, 1975, *Bull. Seismol. Soc. Am.*, *69*(1), 187–205.

Puskas, C. M., R. B. Smith, and C. M. Meertens (2002), GPS-derived models of intraplate deformation of the Yellowstone Hotspot, *Eos Trans. AGU*, *83*(47), Fall Meet. Suppl., Abstract F1037.

Reasenberg, P., and D. H. Oppenheimer (1985), FPFIT, FPPLOT and FPPAGE: FORTRAN computer programs for calculating and displaying earthquake fault-plane solutions, *U.S. Geol. Surv. Open File Rep.*, *85-0739*, 109 pp.

Rivera, L., and A. Cisternas (1990), Stress tensor and fault plane solutions for a population of earthquakes, *Bull. Seismol. Soc. Am.*, *80*(3), 600–614.

Robinson, R., and P. J. McGinty (2000), The enigma of the Arthur's Pass, New Zealand, earthquake. 2: The aftershock distribution and its relation to regional and induced stress fields, *J. Geophys. Res.*, *105*(B7), 16,139–16,150.

Ruppel, E. T. (1972), Geology of pre-Tertiary rocks in the northern part of Yellowstone National Park, Wyoming, in *Geology of Yellowstone National Park*, *U. S. Geol. Surv. Prof. Pap.*, *P 0729-A*, A1–A66.

Savage, J. C., M. Lisowski, W. H. Prescott, and A. M. Pitt (1993), Deformation from 1973 to 1987 in the epicentral area of the 1959 Hebgen Lake, Montana, earthquake (M_S = 7.5), *J. Geophys. Res.*, *98*(B2), 2145–2153.

Smith, R. B., and L. W. Braile (1994), The Yellowstone hotspot, *J. Volcanol. Geotherm. Res.*, *61*(3–4), 121–187.

Smith, R. B., and M. L. Sbar (1974), Contemporary tectonics and seismicity of the western United States with emphasis on the Intermountain Seismic Belt, *Geol. Soc. Am. Bull.*, *85*(8), 1205–1218.

Smith, R. B., and L. J. Siegel (2000), *Windows Into The Earth, The Geologic Story of Yellowstone and Grand Teton National Parks*, Oxford Univ. Press, New York.

Smith, R. B., S. M. Jackson, and W. R. Hackett (1996), Paleoseismology and seismic hazards evaluations in extensional volcanic terrains, *J. Geophys. Res.*, *101*(B3), 6277–6292.

Waite, G. P., and R. B. Smith (2002), Seismic evidence for fluid migration accompanying subsidence of the Yellowstone caldera, *J. Geophys. Res.*, *107*(B9), 2177, doi:10.1029/2001JB000586.

Wessel, P., and W. H. F. Smith (1991), Free software helps map and display data, *Eos Trans. AGU*, *72*(41), 441, 445–446.

Wicks, C. W. J., W. R. Thatcher, and D. Dzurisin (1998), Migration of fluids beneath Yellowstone caldera inferred from Satellite radar interferometry, *Science*, *282*(5388), 458–462.

Zoback, M. L. (1992), First and second-order patterns of stress in the lithosphere: The World Stress Map Project, *J. Geophys. Res.*, *97*(B8), 11,703–11,728.

Zoback, M. L., and M. D. Zoback (1989), Tectonic stress field of the continental United States, in *Geophysical Framework of the Continental United States*, edited by L. C. Pakiser and W. D. Mooney, *Mem. Geol. Soc. Am.*, *172*, 523–539.

R. B. Smith and G. P. Waite, Department of Geology and Geophysics, University of Utah, 135 S. 1460 E., Salt Lake City, UT 84112, USA. (rbsmith@mines.utah.edu; gpwaite@mines.utah.edu)